Journal of Industrial and Engineering Chemistry 43 (2016) 69–77

Contents lists available at ScienceDirect

Journal of Industrial and Engineering Chemistry

journal homepage: www.elsevier.com/locate/jiec

Unique multi-phase Co/Fe/$CoFe_2O_4$ by water–gas shift reaction, CO oxidation and enhanced supercapacitor performances

Seungwon Lee[a], Jung-Soo Kang[b], Kam Tong Leung[b], Wondoo Lee[c], Dongyun Kim[c], Seungyoon Han[c], Wonjun Yoo[c], Hee Jung Yoon[a], Kyusuk Nam[a], Youngku Sohn[a,*]

[a] Department of Chemistry, Yeungnam University, Gyeongsan, Gyeongbuk 38541, South Korea
[b] WATLab and Department of Chemistry, University of Waterloo, Waterloo, ON N2L 3G1, Canada
[c] Daegu Science High School, Daegu 42110, South Korea

ARTICLE INFO

Article history:
Received 30 January 2016
Received in revised form 4 June 2016
Accepted 29 July 2016
Available online 8 August 2016

Keywords:
$Co/Fe/CoFe_2O_4$
Multi crystal-phase
Supercapacitor
Water–gas shift reaction
CO oxidation

ABSTRACT

The design of bimetallic Co–Fe oxide structures has attracted considerable research attention in magnetic, electrochemical and catalyst materials. This paper reports the production of unique multi crystal-phase $Co/Fe/CoFe_2O_4$ by the water–gas shift reaction. The metallic Co and Fe lower the interfacial resistance, resulting in facial charge/ion transport and a dramatic enhancement in the specific capacitance. The multi-phase Co–Fe oxide structures are also found to be applicable to the water–gas shift reaction and CO oxidation. The unique water–gas shift reaction-induced method can be very useful to the design of highly efficient new multi crystal-phase nanostructures.

Introduction

Cobalt (Co) and iron (Fe) have been studied extensively for use as magnetic, electrochemical (e.g., batteries and supercapacitors) and catalytic (e.g., oxygen reduction reaction) materials [1–8]. The efficiency and stability have been enhanced by modifying the morphology and using binary (or ternary) transition metal oxides. Recently, spinel ferrites (MFe_2O_4, M = Co, Fe, Ni, etc.) have attracted considerable research attention [7–22]. A range of methods have been used and diverse morphologies of $CoFe_2O_4$-based materials have been reported, including nanocages [3], mesoporous platelets [4], yolk-shelled nanoprisms [8], nanotubes [10], nanospheres [11], nanofibers [12], hollow structures [13], nanoplates [14], octahedral [14], hierarchical nanoclusters [15], nanoparticles [16,17], mesoporous nanowire arrays [18], and hierarchical flower-like microspheres [19,20]. For applications to energy storage, $CoFe_2O_4$-based materials have been applied in supercapacitors and Li-ion batteries [10–12,15]. A multiphase crystal structure has shown better performance than a single phase structure. Li et al. reported that $CoO/CoFe_2O_4$ nanocomposites could be prepared by annealing CoFe-layered double hydroxides and the battery performance was higher that those of single-phase CoO and $CoFe_2O_4$ [21]. Multiphase crystal structures, consisting of Co, Fe and O include $CoFe_2O_4$/Co [23,24], $CoFe_2O_4/CoFe_2$ [9], $CoO/CoFe_2O_4$ [21], Co/CoO/$CoFe_2O_4$ [25], $Co_3O_4/CoFe_2O_4$ [3], and $Fe_2O_3/CoFe_2O_4$ [26]. The water–gas shift (WGS) reaction ($CO + H_2O \rightarrow CO_2 + H_2$) has been studied extensively for hydrogen production [27,28]. Jeong et al. used spinel ferrite (MFe_2O_4) catalysts (M = Ni, Co, Fe, or Cu) supported on mesoporous alumina for the high temperature (350–550 °C) WGS reaction and reported the optimal catalyst composition [27]. Co–Fe mixed oxides were tested as a good stable CO oxidation catalyst [29–31]. For other catalyst applications, Li et al. synthesized MFe_2O_4 (M = Co, Ni, Cu, Mn) nanofibers and tested the oxygen evolution reaction and H_2O_2 reduction in an alkaline solution, where $CoFe_2O_4$ exhibited the highest catalytic activity [7]. Graphene-supported $Co/CoO/CoFe_2O_4$ was prepared by the thermal decomposition of CoFe-layered double hydroxides and used as an electrocatalyst for the oxygen reduction reaction [25]. $CoFe_2O_4$ has also been reported to be a good electromagnetic wave (e.g., microwave) absorber [25] and a drug-delivery material [20].

In the present study, multi-phase $Co/Fe/CoFe_2O_4$ structures were produced by the WGS reaction, where produced hydrogen at a high temperature was used for the reduction of Co^{2+} (in the octahedral site) and Fe^{3+} (in the tetrahedral site) in $CoFe_2O_4$. Hybridization with metallic Co and/or Fe could be another strategy

* Corresponding author.
E-mail addresses: youngkusohn@ynu.ac.kr, youngkusohn@hotmail.com (Y. Sohn).

http://dx.doi.org/10.1016/j.jiec.2016.07.049
1226-086X/

for enhancing the electrochemical and catalytic properties. The multiphase materials were found to be applicable to the WGS reaction for H_2 production, CO oxidation for the environment and supercapacitors for energy storage.

Experimental

Sample preparation

For the synthesis of Co–Fe precursors, cobalt(II) chloride ($CoCl_2{\cdot}6H_2O$, 98%, Sigma–Aldrich) and ferrous(II) chloride ($FeCl_2{\cdot}4H_2O$, 98%, Sigma–Aldrich) were first dissolved completely in 40 mL deionized water. For the synthesis of two different samples, the molar quantities of Co/Fe were set at 0.027 mol/0.013 mol and 0.013 mol/0.027 mol. Upon complete dissolution, 2.0 mL of a 1.0 M NaOH solution was added to each of the solutions to obtain precipitates. The solution in a Teflon bottle was sealed tightly and placed in an oven, which was set at 120 °C. The reaction time was fixed to 12 h. After the hydrothermal reaction, the bottle was cooled naturally to room temperature and opened. The final powder products were collected by centrifugation followed by washing with deionized water and ethanol. These washing and centrifugation steps were repeated several times. The samples collected in a vial were dried in an oven at 80 °C for several days. The dried as-prepared samples were used in the CO oxidation and water–gas shift (WGS) reactions. The as-prepared samples were annealed thermally at 600 °C for 3 h. To clarify the samples, the two as-prepared samples were designated, A_{as} and B_{as}, respectively. The annealed samples were designated, A_{an} and B_{an}, respectively.

Sample characterization

All powder samples before and after the catalyst tests were examined by field-emission scanning electron microscopy (SEM, Hitachi S-4800) at an acceleration voltage range of 5–20 keV. To obtain the SEM images, the powder samples were mounted on a small Si substrate. Energy dispersive X-ray (EDX) spectroscopy was employed using a Hitachi S-4200 FE-SEM/EDX. The crystal phase before and after the sample treatments were examined by X-ray diffraction (XRD, PANalytical X'Pert Pro MPD) using Cu Kα radiation (40 kV and 30 mA) at a take-off angle of 6°. The change in chemical composition after the WGS reaction was examined clearly by X-ray photoelectron spectroscopy (XPS, Thermo-VG Scientific K-Alpha) equipped with a hemispherical electron energy analyzer and a monochromatic Al Kα X-ray (1486.6 eV) source. Optical microscopy images were obtained to examine the colors of the samples. Fourier Transform Infrared (FTIR, Thermo Scientific Nicolet iS10) spectroscopy was performed in diamond attenuated total reflectance mode over the wavenumber range, 600–4000 cm^{-1}, with a resolution of 4 cm^{-1}. A Bruker Senterra Raman spectrometer was employed to measure the Raman spectra with a 532 nm laser light source. The magnetization curves of the samples were obtained using a MPMS SQUID magnetometer (Quantum Design, USA) with a magnetic field between −70 and 70 kOe at temperatures of 1.8, 5, 77, and 300 K. The temperature dependent magnetization was measured in zero field cooling (ZFC) and field cooled cooling (FCC) modes.

WGS and CO oxidation reactions

For the WGS reaction, 20 mg of the as-prepared powder samples were loaded into a quartz U-tube with an inner diameter of 4 mm. A mixture gas of 5% CO/N_2 gas was introduced to the sample with water vapor. The reaction products of CO_2 and H_2O were monitored using a RGA200 (Stanford Research Systems) mass spectrometer. The temperature heating rate over the sample was 10 °C min^{-1}. For CO oxidation, a mixture gas of CO (1.0%)/O_2 (2.5%)/N_2 was introduced. The other conditions were the same as those for the WGS reaction. The samples after CO oxidation were designated, A_{CO} and B_{CO}, and after the water–gas shift reactions as A_{WGS} and B_{WGS}.

Electrochemical measurements

All the electrochemical experiments, such as cyclic voltammetry (CV), chronopotentiometry (CP) and impedance measurements, were performed in a three-electrode system with a working electrode, a Pt wire counter electrode and a Ag/AgCl reference electrode using a CH Instruments 660D electrochemical workstation. The working electrode was prepared as follows. A blend containing 60 wt.% of the samples, 20 wt.% of carbon black (a conducting agent) and 20 wt.% polyvinylidene fluoride (PVDF, a binder) was mixed in *N*-methyl-2-pyrrolidone (NMP) solvent. The materials dispersed in the solution were embedded uniformly in a Ni foam and fully dried. The Ni foam was pellet-pressed to make a working electrode. A 6 M KOH aqueous solution was used as the electrolyte.

Results and discussion

Fig. 1 shows SEM images of the as-prepared (A_{as} and B_{as}) and annealed (A_{an} and B_{an}) samples, as well as the samples (A_{WGS} and B_{WGS}) after the water–gas shift (WGS) reactions. The as-prepared A_{as} and B_{as} samples showed hexagonal plate (150–300 nm) and nanocube (10–60 nm) morphologies, respectively. The corresponding TEM image of the smaller size B_{as} sample clearly showed sizes and the morphology (Supporting information, Fig. S1). The as-prepared sample A (A_{as}) was dark yellow and non-magnetic while the as-prepared sample B (B_{as}) was black and magnetic. The $Co(OH)_2$ precursors were pink-colored with a hexagonal platelet morphology. The $Fe(OH)_2$ precursors were reported to be white [32]. For this reason, the in dark yellow hexagonal plates were not $Co(OH)_2$ and/or $Fe(OH)_2$. Upon annealing, the colors and morphologies changed significantly. The hexagonal plates changed to the morphology of fibrous structures (A_{an}) upon annealing. The color (dark yellow) was changed to gray/black and the particles became magnetic. The nanocubes (B_{as}) were aggregated to form larger particles (B_{an}) and were darker in color (also see Supporting information, Fig. S1). The magnetic properties were still present. After the WGS reactions, all the particles (A_{WGS} and B_{WGS}) became more irregular in size and shape. Elongated protrusions are seen from the A sample after WGS reaction. The hexagonal plates (A_{WGS}) and nanocubes (B_{WGS}) were lighter in color (black → dark gray), compared to the corresponding annealed samples (A_{an} and B_{an}). Based on the EDX data, the A and B samples were Co-rich and Fe-rich, respectively. Sample A showed that the concentration of Co was approximately two times higher than Fe. On the other hand, in sample B, the concentration of Fe was approximately two times higher than Co. Elemental percentages (%) are provided in the Supporting information, Table S1, compared with those measured using XRD and XPS. The amount of oxygen was reduced after the WGS reaction, suggesting that the oxide forms were reduced. Karipoth et al. prepared FeCo particles in ethylene glycol with NaOH at 180 °C using a polyol synthesis method. They reported that the Fe-rich and Co-rich particles were more like cubes and inter-connected spherical particles, respectively [33]. This was consistent with the present study.

Various samples with different colors and different magnetic properties were examined by XRD. In the as-prepared sample A (A_{as}), the XRD peak positions were very close to those of hexagonal (R-3m) cobalt (and iron) hydroxide chloride hydrate (JCPDS 98-008-2450). The peaks at $2\theta = 11.3°$ and 22.7° were assigned to the

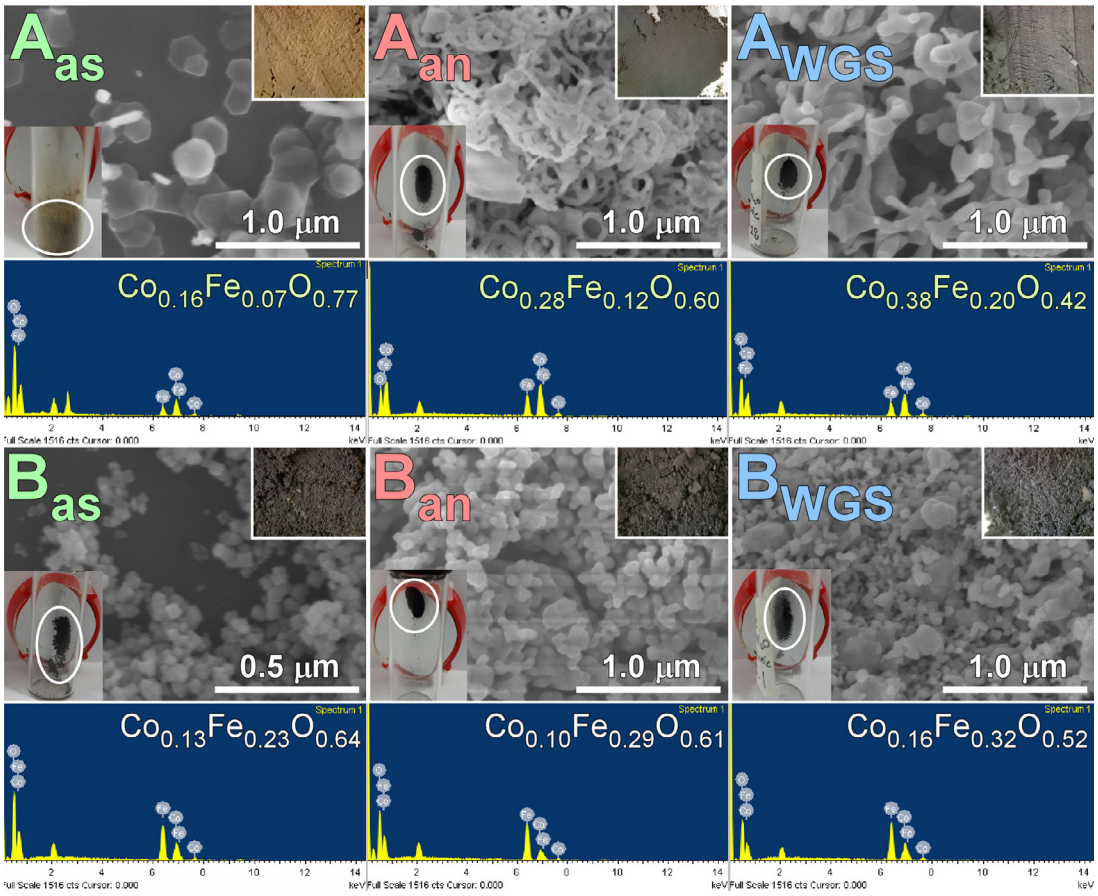

Fig. 1. SEM images and corresponding EDX data of the as-prepared (A_{as} and B_{as}), annealed (A_{an} and B_{an}) and WGS reaction (A_{WGS} and B_{WGS}) samples. Each inset photo shows the color of the corresponding samples. The five gray/black color samples were attracted by a magnet.

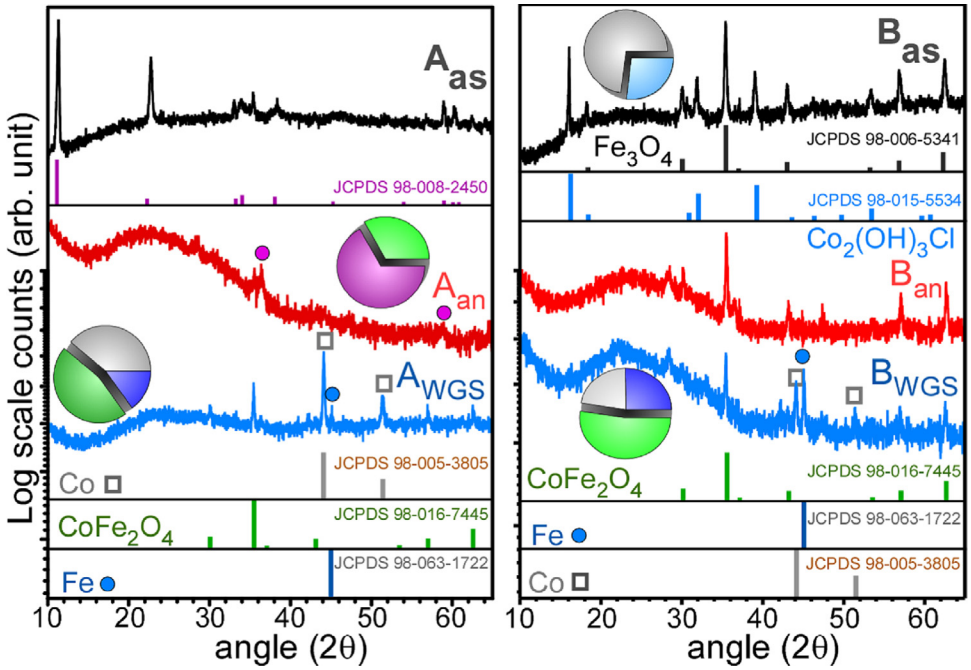

Fig. 2. Powder XRD patterns of the as-prepared (A_{as} and B_{as}), annealed (A_{an} and B_{an}) and WGS reaction (A_{WGS} and B_{WGS}) samples. The reference XRD patterns are also shown. The insets show the relative compositions of the multi phases.

(0 0 3) and (0 0 6) planes, respectively. The peak intensity at $2\theta = 22.7^\circ$ was stronger than the reference pattern, which was attributed to an unassigned Fe complex. A broad FT-IR peak was observed at 3450 cm^{-1}, which was assigned to the vibration modes of OH and hydrate (Supporting information, Fig. S2) [32]. The strong peak at approximately 670 cm^{-1} was due to the Fe—O (and Co—O) stretching vibration modes. Similarly, Zhang et al. reported hexagonal cobalt ferrous hydroxide ($Co_xFe_{1-x}(OH)_2$) crystal sheets (~6 μm wide and 50–200 nm thick) by a precipitation method at 100 °C using the same Co and Fe chloride precursors with hexamethylenetetramine [4]. They observed a strong XRD peak at $2\theta = 19.1^\circ$, which was assigned to the (0 0 1) plane of the brucite-like structure. After thermal annealing, the XRD peaks became significantly weaker due to less crystalline state. On the other hand, the weak XRD peaks could be resolved into two different crystal phases of Co_3O_4 and $CoFe_2O_4$ [12,21,34]. The weak peaks at approximately $2\theta = 35.5^\circ$ and 36.5° were attributed to the (1 1 3) plane of cubic (Fm-3m) $CoFe_2O_4$ (JCPDS 98-016-7445) and the (1 1 3) plane of cubic (Fm-3m) Co_3O_4 (JCPDS 98-006-9377), respectively. The multi-phase $Co_3O_4/CoFe_2O_4$ structures were prepared by thermal annealing method [12,34], which is consistent with the present study. Rai et al. prepared a multi-phase $Co_3O_4/CoFe_2O_4$ nanocomposite by the thermal annealing (at 700 and 900 °C) of a single-phase $CoFe_2O_4$ material, and reported that the multi-phase showed superior Li-ion battery performance to the single-phase [34]. After the water–gas shift reaction (A_{WGS}), the XRD patterns changed distinctly and were resolved into three crystal phases, cubic (Fm-3m) metallic Co (JCPDS 98-005-3805), cubic (Fm-3m) $CoFe_2O_4$ (JCPDS 98-016-7445) and cubic (Im-3m) metallic Fe (JCPDS 98-063-1722). For the multi crystal-phase Co/Fe/$CoFe_2O_4$ material, the composition ratio of the Co-rich sample was estimated to be $CoFe_2O_4$ (46%), Co (39%) and Fe (15%). Under hydrogen reducing conditions at 290–400 °C, the $CoFe_2O_4$ nanofibers changed to multiphase $CoFe_2O_4/CoFe_2$ nanocomposites [9]. Based on the literature and the present result, the Co/Fe/$CoFe_2O_4$ structures could be prepared by a water–gas shift reaction.

The XRD patterns of the as-prepared sample B (B_{as}) could be resolved into two crystal phases. One was attributed to hexagonal (R-3m) dicobalt chloride trihydroxide, $Co_2(OH)_3Cl$ (JCPDS 98-015-5534). A sharp FT-IR peak was observed at 3560 cm^{-1}, which was assigned to the OH stretching mode of $Co_2(OH)_3Cl$ (Supporting information, Fig. S2) [32]. The strong peak at approximately 600 cm^{-1} was attributed mainly to Co—O (and Fe—O) vibration modes. The other crystal phase was probably due to cubic (Fd-3m) Fe_3O_4 (JCPDS 98-006-5341) and/or cubic (Fm-3m) $CoFe_2O_4$ (JCPDS 98-016-7445). The dark color and the magnetic property (Fig. 1) of the as-prepared sample originated presumably from the properties of Fe_3O_4 and/or $CoFe_2O_4$. After annealing the sample (B_{an}), the XRD peaks for $Co_2(OH)_3Cl$ disappeared and only the XRD peaks of the oxide were present. As a consequence, the powder sample became darker (Fig. 1). Upon the WGS reaction, the XRD revealed three crystal phases of Co, $CoFe_2O_4$ and Fe, as observed for A_{WGS}. On the other hand, the composition ratio was different; $CoFe_2O_4$ (53%), Co (22%) and Fe (25%), where the Fe concentration was higher than Co. The three crystal phase Co/Fe/$CoFe_2O_4$ could be obtained not by thermal annealing but the WGS reaction.

Fig. 3 presents the mass ($CO_2 = 44$ amu, $CH_4 = 16$ amu and $H_2 = 2$ amu) profiles of the as-prepared A_{as} and B_{as} samples commonly observed during the first and second run WGS reactions. A qualitative comparison of the two samples could identify an efficient way to design more useful WGS reaction catalysts. The first run was performed using the as-prepared samples up to 600 °C. The second run was the sample, which was already experienced the first run. For this reason, the sample in the second run was a stabilized sample. In the first run of the as-

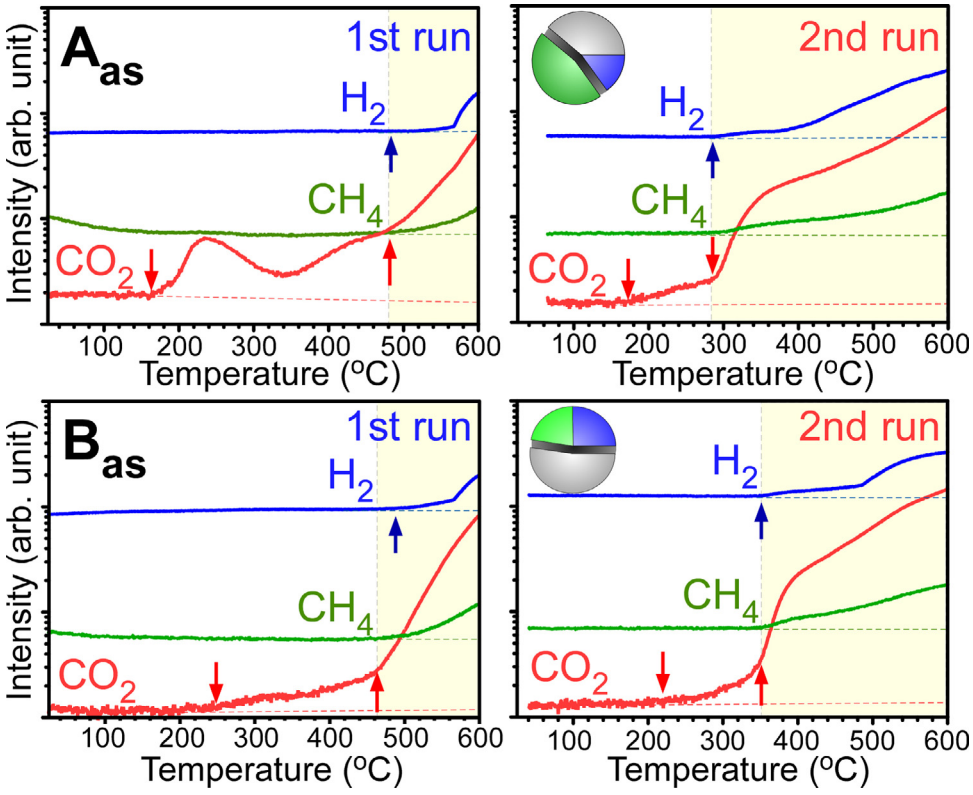

Fig. 3. Qualitative comparison of the WGS reaction mass ($CO_2 = 44$ amu, $CH_4 = 16$ amu and $H_2 = 2$ amu) profiles for the as-prepared A_{as} and B_{as} samples. The samples after the second run were designated as A_{WGS} and B_{WGS}, as mentioned above. As shown in the insets, the crystal phases changed after the WGS reaction. The onset temperatures are indicated by the arrows.

prepared Co-rich sample (A_{as}), CO_2 was detected starting from 160 °C. No H_2 and CH_4 signals were detected between 160 and 480 °C. The CO_2 signal intensity initially increased and then decreased from 240 °C. The signal increased again from 340 °C. The rise and fall of the CO_2 signal could be related to the decomposition of the precursor (A_{as}). At 480 °C, the slope of the CO_2 signal profile changed and increased linearly. Interestingly, both H_2 and CH_4 signals were also detected. This suggests that the WGS reaction process started from this temperature, where several reaction mechanisms were involved, such as $H_2O_{ad} \rightarrow H_{ad} + OH_{ad}$, $CO_{ad} + OH_{ad} \rightarrow CO_2(g) + H_{ad}$ and $H_{ad} + H_{ad} \rightarrow H_2(g)$. CH_4 formation is an undesirable side reaction and is formed via $CO + 3H_2 \rightarrow CH_4 + H_2O$ or $CO + H_2 \rightarrow 1/2CH_4 + 1/2CO_2$. CH_4 formation is suppressed by modifying the nature of the catalyst [27,35,36]. On the other hand, this modification was beyond the scope of the present study. In the second run, the CO_2 signal showed no fluctuations because the Co–Fe complex decomposed to form a more stable crystal structure. The rise of a weak CO_2 signal between 180 °C and 280 °C was attributed to $CO + O$ (surface oxygen) $\rightarrow CO_2(g)$. The consumption of surface oxygen was confirmed by EDX (Fig. 1). The CO_2 signal increased drastically from 280 °C, where the H_2 and CH_4 signals stated to rise. This was explained by the WGS reaction and the activity was increased substantially. For the first run of the as-prepared Fe-rich sample (B_{as}), the CO_2 signal started from 245 °C, which was much lower than that for sample A_{as}. The H_2 and CH_4 signals stated to increase from 460 °C. In the second run, the CO_2 signal was detected from 220 °C. A drastic increase in CO_2 was observed from 280 °C, where the H_2 and CH_4 signals also appeared. Compared to the second run for the Co-rich sample A, the Fe-rich sample B showed poor catalytic activity for the WGS reaction.

The magnetic properties of the selected samples were examined. The magnetization with an applied magnetic field (M–H) was examined by SQUID and displayed in Fig. 4. The temperature dependent magnetization in the field-cooled-cooling (FCC) and zero-field-cooling (ZFC) modes was measured at an applied magnetic field of H = 1000 Oe (1.0 kOe) over the temperature range, 1.8–300 K. A magnetic hysteresis loop was commonly observed (Supporting information, Fig. S3), indicating the ferromagnetic properties of the materials. The wideness of the loop was in the order of $A_{WGS} < B_{WGS} < A_{an}$. The loop of the annealed A sample (A_{an}) was not perfectly smooth, indicating multi-phase structures. The magnetization curves commonly became saturated

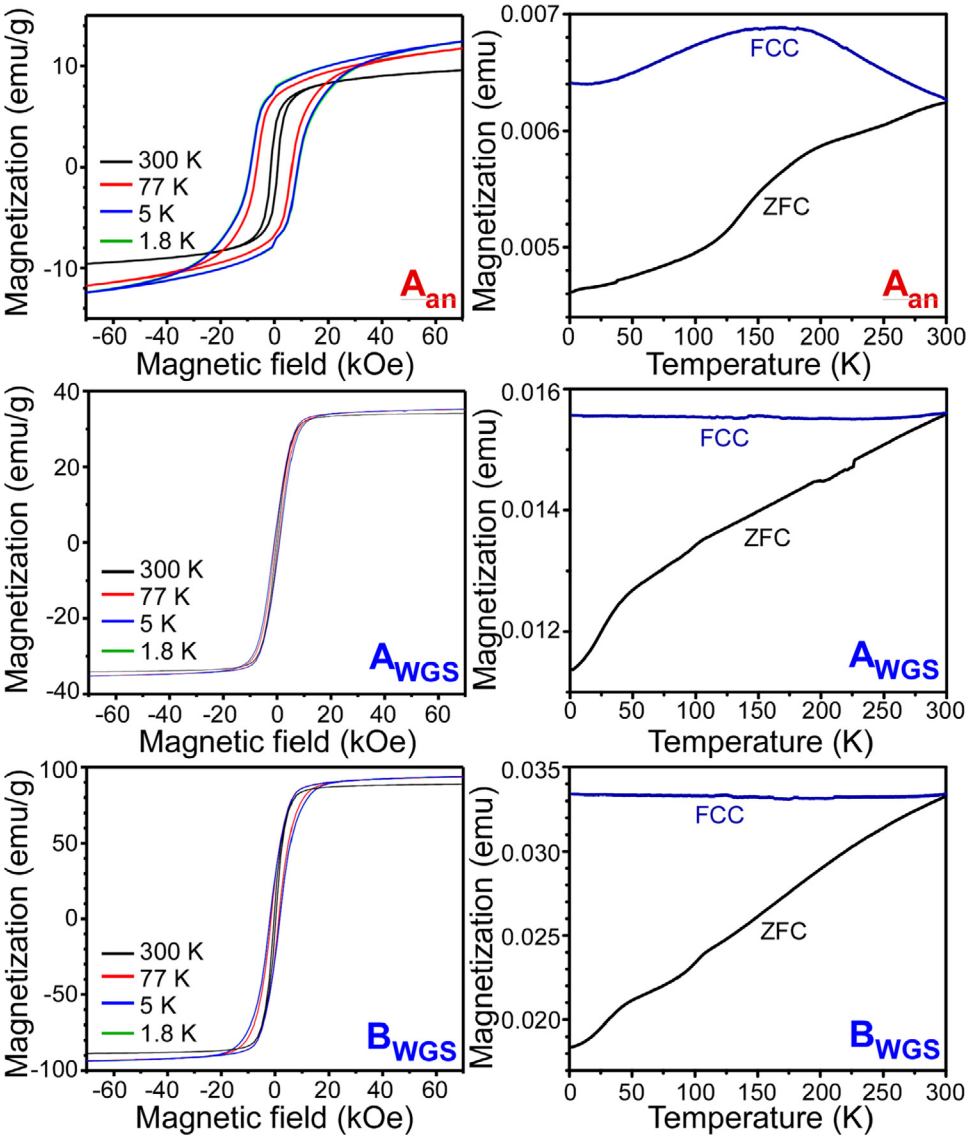

Fig. 4. Magnetization (M–H) curves (left column) at 1.8, 5, 77, and 300 K for the annealed sample A (A_{an}) and post-WGS reaction A and B samples (A_{WGS} and B_{WGS}). Magnetization with temperature in the FCW, FCC and ZFC modes (right column) taken at 1.0 kOe. The data taken at 5 K and 1.8 K were exactly superimposable.

with increasing applied magnetic field. For the annealed sample A (A_{an}) with less crystalline multiphase $Co_3O_4/CoFe_2O_4$ structures, the measured coercivities were 1.2, 6.4, 8.5, and 8.6 kOe at 300 K, 77 K, 5 K, and 1.8 K, respectively. The saturation magnetization values were 9.6, 11.7 and 12.4 emu g^{-1} at 300 K, 77 K and 5 K/1.8 K, respectively. The FCC curves first increased and then decreased with decreasing temperature, with a broad maximum at approximately 170 K. This was attributed to the interparticle interactions. The FCC and ZFC curves were not met and split over the measured temperature range. For the Co-rich sample A after the WGS reaction (A_{WGS}), the measured saturation magnetization values were 33.5, 34.3 and 34.4 emu g^{-1} at 300 K, 77 K and 5 K/1.8 K, respectively. For the Fe-rich sample B after the WGS reaction (B_{WGS}), the magnetization was increased substantially and the saturation magnetization values were measured to be 88.7, 93.5 and 93.7 emu g^{-1} at 300 K, 77 K and 5 K/1.8 K, respectively. Choi et al. reported a saturation magnetization of 62.3 emu g^{-1} for $CoFe_2O_4$ nanoparticles (~10 nm) [37]. Zan et al. synthesized a $CoFe_2O_4/Co_{0.7}Fe_{0.3}$ nanocomposite by a hydrothermal method and measured the maximum magnetization of 88.9 emu/g and a coercivity of 0.3 kOe [38]. Clifford et al. synthesized $Fe_{60}Co_{40}$ alloys and reported a saturation magnetization of 205 emu g^{-1} at 300 K, which was increased by the Co-loading [39]. The FC and ZFC curves for the A_{WGS} and B_{WGS} samples exhibited similar behavior, indicating that they were the same materials. As discussed above, the A_{WGS} and B_{WGS} samples are $Co/Fe/CoFe_2O_4$, but with different composition ratios. The FC curves showed similar values with temperature while the ZFC decreased gradually with decreasing temperature.

The chemical states of the samples after the WGS reaction were examined by X-ray photoelectron spectroscopy (XPS). The annealed sample (A_{an}) was selected for comparison. Fig. 5 presents the survey Co 2p, Fe 2p, and O 1s XPS spectra. A typical survey spectrum (including other survey spectra) showed the elements of Co, Fe, O, and C (Supporting information, Fig. S4). The C 1s peak at ~285.0 eV was attributed to impurity carbon. Asymmetric Co $2p_{3/2}$ and Co $2p_{1/2}$ XPS peaks were observed at 779.8 and 794.9 eV, respectively, with a measured spin-orbit (S-O) splitting energy of 15.1 eV. These were in good agreement with the literature binding energy values for the mixed-valence (Co^{2+} and Co^{3+}) Co_3O_4. The strong/broad satellite peaks at 786.4 and 802.5 eV were assigned to the presence of Co^{2+}. The Co^{2+} could be also due to $CoFe_2O_4$. The annealed sample A (A_{an}) was assigned to multi-phase $Co_3O_4/CoFe_2O_4$ based on the XRD patterns (Fig. 2). For the Fe 2p XPS of the annealed Co-rich sample (A_{an}), broad Fe $2p_{3/2}$ and Fe $2p_{1/2}$ peaks were observed at 711.1 eV and 724.8 eV, respectively, with a spin-orbit splitting of 13.7 eV. This was attributed to Fe^{3+} in $CoFe_2O_4$ and/or FeOOH-related species [40]. The shake up satellite peaks (at ~718.4 and ~732.9 eV) were clearly observed, which is indicative of the presence of Fe^{3+} [4]. The corresponding O 1s peaks were observed at 529.7, 532.8 and 533.3 eV, which were attributed to the lattice oxygen of metal oxides, chemisorbed oxygen (M–OH) and O=C—OH species, respectively [30]. The C 1s XPS peaks support the presence of O=C—OH and C—OH species (Supporting information, Fig. S4). All the curve-fitting XPS spectra and the relative percentage of each peak are provided in the Supporting information, Fig. S4.

For the samples after the WGS reactions (A_{WGS} and B_{WGS}), the XPS peaks became critically different from those of the thermal-annealed sample. The A_{WGS} and B_{WGS} samples showed the same Co 2p and Fe 2p XPS profiles. The Co $2p_{3/2}$ (Co $2p_{1/2}$) XPS peak was observed at 780.4 eV (796.4 eV) with a S-O splitting energy of 16.0 eV, which is much wider than that (15.1 eV) of the annealed sample. In addition, two shakeup satellite peaks became significantly stronger and were observed at 786.4 and 802.5 eV, which indicates the significant presence of high spin Co^{2+} [4,30,41]. The

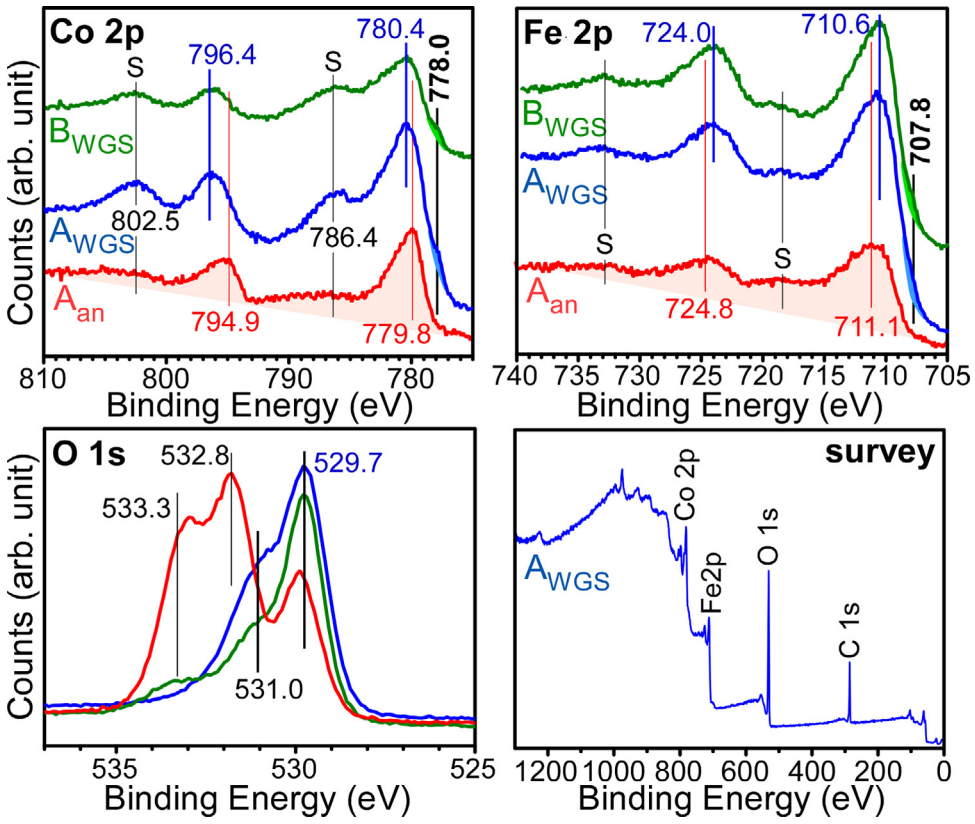

Fig. 5. Co 2p, Fe 2p, O 1s, and survey XPS spectra of the annealed sample (A_{an}), and the samples (A_{WGS} and B_{WGS}) after the WGS reaction. A survey spectrum of the A_{WGS} sample is only shown for clarity.

satellite signals were enhanced after the WGS reaction. Based on the XRD (Fig. 2) and XPS results, the Co 2p and satellite signals could be assigned to Co(II)-O species of $CoFe_2O_4$ [25]. Interestingly, a new Co 2p XPS peak appeared at 778.0 eV, which was attributed to metallic Co [23,25]. The Fe $2p_{3/2}$ and Fe $2p_{1/2}$ peaks were observed at 710.6 eV and 723.0 eV, respectively. This was attributed to Fe^{3+} of $CoFe_2O_4$. The shake-up satellite peaks were observed at 718.2 and 732.8 eV, confirming the presence of Fe^{3+} [15]. A new shoulder Fe $2p_{3/2}$ peak was clearly observed at 707.8 eV upon the water–gas shift reaction, which was attributed to the metallic Fe. Metallic Co and Fe were already confirmed by XRD (Fig. 2). Although the XRD results showed very strong metallic Fe and Co, surface sensitive XPS showed weaker metallic Co 2p and Fe 2p peaks due to the surface oxidation of Co and Fe, respectively. The Co-rich sample (A_{WGS}) showed a stronger Co 2p XPS signal than that of the Fe-rich (B_{WGS}). On the other hand, the Fe-rich sample (B_{WGS}) showed a stronger Fe 2p XPS signal than that of the Co-rich sample (A_{WGS}). The corresponding O 1s peaks were observed at 529.7 and 531.0 eV, which were attributed to lattice oxygen and chemisorbed oxygen (M–OH)/oxygen vacancies (O^- and O_2^-), respectively [30].

Fig. 6 displays the cyclic voltammetry (CV) curves of the annealed samples (A_{an}, and B_{an}) and samples after the WGS reaction (A_{WGS} and B_{WGS}). The broad anodic and cathodic peaks were assigned to the electrochemical redox reactions of Co and Fe ions. The anodic and cathodic peak currents increased with increasing scan rate. The plots of the current versus the square root of the scan rate showed a good linear relationship (Supporting information, Fig. S5). The change in slope was in the order of $A_{an}(A_{WGS}) < C_{an}(C_{WGS}) < B_{an}(B_{WGS})$. The oxidation and reduction peak positions and the gap ($\Delta E_p = E_{pa} - E_{pc}$) also increased linearly with increasing scan rate, indicating a diffusion-controlled process in the electrode reaction system.

The charge–discharge measurements (Fig. 6) with different current densities (0.83, 1.67, 3.3, and 8.3 A g^{-1}) were performed with a fixed potential range of 0.0–0.4 V. The charge–discharge time increased with decreasing current density. At a fixed current density of 0.83 A g^{-1}, the charge/discharge time was measured to be 18 s for the annealed Co-rich sample (A_{an}). The time was increased dramatically to 380 s after the WGS reaction (A_{WGS}). For the annealed Fe-rich (B_{an}) and WGS reaction (B_{WGS}) samples, the charge/discharge time was measured to be 83 and 92 s at a fixed current density of 0.83 A g^{-1}, respectively. The Nyquist plots (Fig. 6) showing the real (Z') and imaginary (Z'') parts of the impedance of the annealed (A_{an} and B_{an}) and WGS reaction (A_{WGS} and B_{WGS}) samples were examined. The real (Z') part commonly decreased with increasing frequency. For the annealed sample A (A_{an}), a single semicircle and a straight line were observed in the high and

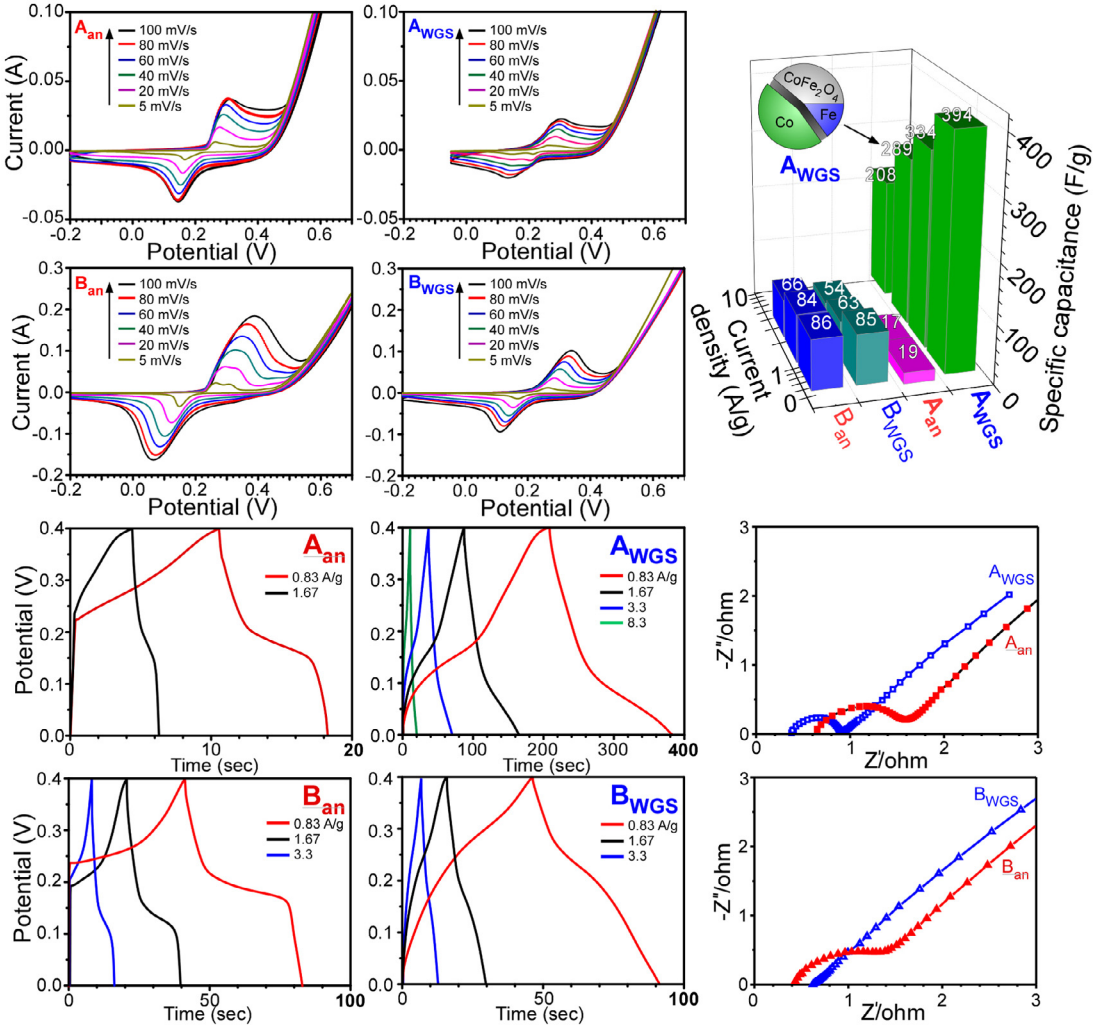

Fig. 6. CV curves with different scan rates (top left), charge–discharge curves with different charge currents (bottom left), the corresponding frequency dependence impedance plots (bottom right), and calculated specific capacitance with the current density (top right) for the annealed (A_{an} and B_{an}) and WGS reaction (A_{WGS} and B_{WGS}) samples. The inset (top right) shows the composition of the sample A after the WGS reaction (A_{WGS}).

low frequency regions, respectively. The other two annealed samples (B_{an} and C_{an}) also showed a high frequency semicircle, which was attributed to the grain-boundary contribution. The magnitude of the radius showed an order of $A_{an} < B_{an}$. The single phase structure showed a lower grain-boundary conduction. For the sample after the WGS reaction (A_{WGS}), the radius of the semicircle became smaller. The semicircle almost disappeared for the other two samples after the WGS reaction, indicating a lower interfacial (electrode/electrolyte) electrochemical reaction resistance [42]. The solution/charge transfer resistance was measured to be 1.6 Ω and 0.9 Ω for the annealed (A_{an}) and WGS reaction (A_{WGS}) samples, respectively. For annealed (B_{an}) and WGS reaction (B_{WGS}) samples, the resistance was measured to be 1.6 Ω and 0.6 Ω, respectively. The lower resistance was observed after the WGS reaction. In the multi-phase Co/Fe/$CoFe_2O_4$ structures, the conductivity was improved by the metallic Co and Fe to result in efficient charge/ion transport and high charge storage [42]. The incorporation of graphene (or carbon) has also been used extensively to reduce the interfacial charge transfer resistance [15,43–46].

The specific capacitance ($F\,g^{-1}$) was calculated using the equation: $C = (I \times t)/\Delta V$, where I is the discharge current density ($A\,g^{-1}$), t is the discharge time, and ΔV is the potential range [47–49]. The calculated specific capacitances are displayed in Fig. 6. For the annealed Co-rich sample A (A_{an}), the specific capacitances were calculated to be 19 and 17 $F\,g^{-1}$ at current densities of 0.83 and 1.67 $A\,g^{-1}$, respectively. The specific capacitance was increased dramatically (20×) after the WGS reaction (A_{WGS}) and was calculated to be 394, 334, 289, and 208 $F\,g^{-1}$ at current densities of 0.83, 1.67, 3.3, and 8.3 $A\,g^{-1}$, respectively. For the annealed sample B (B_{an}), the specific capacitances were calculated to be 86, 84 and 66 $F\,g^{-1}$ at current densities of 0.83, 1.67 and 3.3 $A\,g^{-1}$, respectively. After the WGS reaction (B_{WGS}), the values were similar, unlike the sample A_{an}. Based on the specific capacitance, the Co-rich multi-phase structure ($CoFe_2O_4$:Co:Fe = 46%:39%:15%) showed a dramatic increase in efficiency for supercapacitor applications.

The CO oxidation [50–56] by Co–Fe oxides is an attractive topic for air purification [29,30]. The as-prepared Co-rich sample (A_{as}) was selected to test the CO oxidation activity with temperature, which is displayed in Fig. 7. The temperature at 10% CO conversion was designated as $T_{10\%}$. In the first run, the CO oxidation activity began to appear at 185 °C and $T_{10\%}$ was observed at 205 °C. The CO oxidation first increased from 185 °C, decreased from 240 °C and then increased again from 330 °C. A similar CO oxidation profile

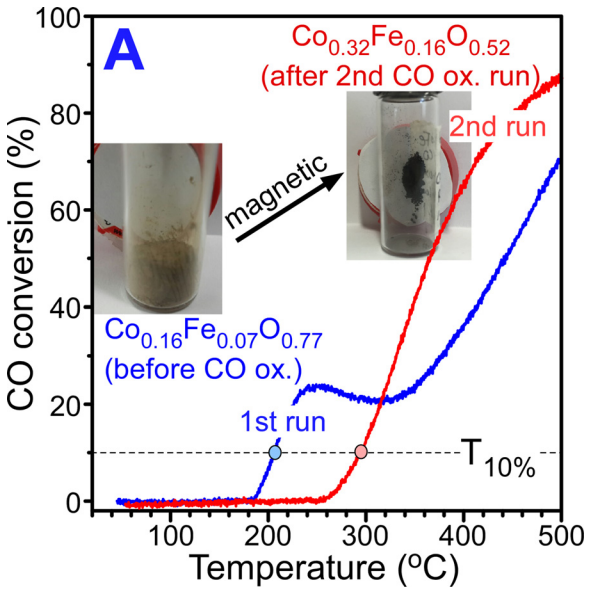

Fig. 7. First and second run CO conversion (%) profiles with the reaction temperature for the Co-rich sample A. The insets show photographs indicating the magnetic properties (and the colors) before and after CO oxidation.

was also observed during the WGS reaction (Fig. 3). This was attributed to decomposition of the Co–Fe complex. In the second run, the CO oxidation onset was observed at 260 °C and $T_{10\%}$ = 295 °C. Kouotou et al. reported $T_{10\%}$ = 170–215 °C for CO oxidation over Co–Fe oxides [30], which is higher CO oxidation activity compared to the present study. After CO oxidation, the sample became black and magnetic and the composition had changed, as discussed above.

After the CO oxidation of the Co-rich sample, the crystal phase was examined by XRD. The XRD peaks were broader and asymmetrical. A major asymmetric peak was observed at $2\theta = 36.3°$. The XRD patterns were in good agreement with those of cubic (Fd-3m) Co_2FeO_4 (JCPDS 98-009-8552) and the broader peaks could be resolved into other similar crystal phases (e.g., Fe_3O_4 and Co_3O_4), as shown in Fig. 8. The composition of Co/Fe/O was determined by EDX to be 32%/16%/52%. The color of the sample was gray/black and the SEM image revealed morphology of clustered particles. Several strong FT-IR peaks were observed between 600–700 cm^{-1}, which were attributed to the stretching vibration modes of metal–oxygen (Fe—O and Co—O) bonds in the

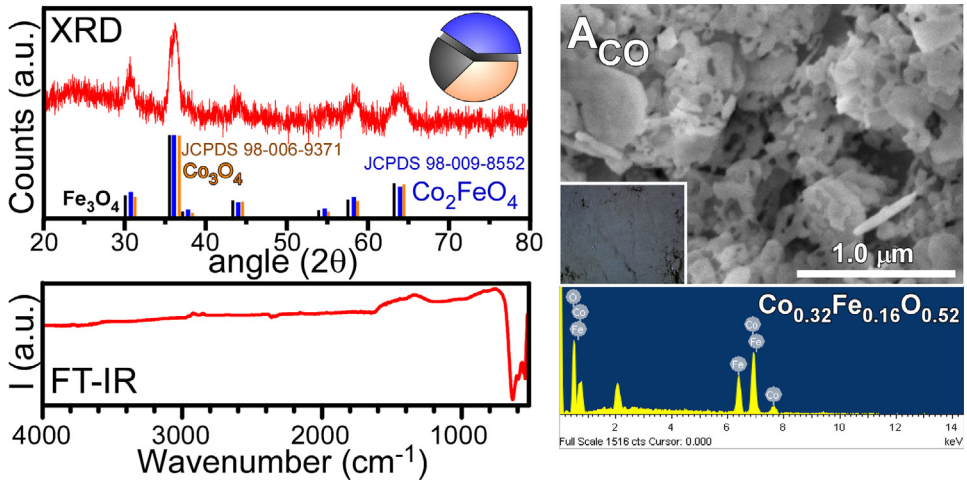

Fig. 8. XRD (top left), SEM (top right), FT-IR (bottom left), and EDX (bottom right) taken for the Co-rich sample A after CO oxidation.

crystalline lattices [28]. The peak positions were also dependent on the occupied positions (tetrahedral or octahedral) of metal ions. The metal ion in an octahedral site generally has a lower vibration wavenumber than that in a tetrahedral site [28].

We obtained the CV curves and plots of the current versus the square root of the scan rate (Supporting information, Fig. S6). The change in current with increasing scan rate showed a linear relationship, indicating a diffusion-controlled electrochemical reaction process. The specific capacitances were calculated to be 102, 71 and 33 $F\,g^{-1}$ at current densities of 0.83, 1.67 and 3.3 $A\,g^{-1}$, respectively. The specific capacitance was improved compared to that of the annealed sample (A_{an}). Based on the Nyquist plot, the magnitude of the semicircle was smaller than that of the annealed sample (A_{an}). The solution/charge transfer resistance was measured to be 1.0 Ω for the sample (A_{CO}) after CO oxidation.

Conclusions

Multi crystal-phase Co-rich Co/Fe/$CoFe_2O_4$ could be produced by the WGS reaction. The phases were confirmed by XRD and XPS. The Co-rich multi-phase showed 4–20× superior supercapacitor performance than the Fe-rich Co/Fe/$CoFe_2O_4$ and multiphase Co–Fe oxides. The metallic Co and Fe improved the conductivity, which increased charge/ion transport and resulted in high charge storage. The Co-rich and Fe-rich Co/Fe/$CoFe_2O_4$ structures showed saturation magnetization of 34 and 94 emu/g, respectively. The Co-rich Co/Fe/$CoFe_2O_4$ showed a WGS reaction onset at 280 °C with the formation of H_2O, CO_2 and CH_4 (by product). The onset temperature was much lower than that (350 °C) of the Fe-rich Co/Fe/$CoFe_2O_4$. The multi-phase Co–Fe oxides also showed a potential applicability to CO oxidation with an onset temperature of 250 °C. The wide application tests of Co–Fe oxides and the unique design of multi-phase Co/Fe/$CoFe_2O_4$ solely by the WGS reaction could be very practical for the development of Co–Fe-based materials.

Acknowledgements

This study was supported financially by Daegu Science High School R&E Program in 2015 and by the National Research Foundation of Korea (NRF) grant funded by the Korea government (MEST) (NRF-2014R1A1A2055923).

Appendix A. Supplementary data

Supplementary data associated with this article can be found, in the online version, at http://dx.doi.org/10.1016/j.jiec.2016.07.049.

References

[1] C.Z. Yuan, H.B. Wu, Y. Xie, X.W. Lou, Angew. Chem. Int. Ed. 53 (2014) 1488.
[2] Z. Ma, Curr. Catal. 3 (2014) 15.
[3] H. Hu, B. Guan, B. Xia, X.W. Lou, J. Am. Chem. Soc. 137 (2015) 5590.
[4] Z. Zhang, W. Li, R. Zou, W. Kang, Y.S. Chui, M.F. Yuen, C.-S. Lee, W. Zhang, J. Mater. Chem. A 3 (2015) 6990.
[5] P. Hu, M. Long, Appl. Catal. B 181 (2016) 103.
[6] S. Khilari, S. Pandit, J.L. Varanasi, D. Das, D. Pradhan, ACS Appl. Mater. Interfaces 7 (2015) 20657.
[7] M. Li, Y. Xiong, X. Liu, X. Bo, Y. Zhang, C. Han, L. Guo, Nanoscale 7 (2015) 8920.
[8] L. Yu, B.Y. Guan, W. Xiao, X.W. Lou, Adv. Energy Mater. 5 (2015) 1500981.
[9] J. Xiang, X. Zhang, J. Li, Y. Chu, X. Shen, Chem. Phys. Lett. 576 (2013) 39.
[10] X. Zhang, Y. Xie, Y. Sun, Q. Zhang, Q. Zhu, D. Hou, J. Guo, RSC Adv. 5 (2015) 29837.
[11] L. Liu, Z. Hu, L. Sun, G. Gao, X. Liu, RSC Adv. 5 (2015) 36575.
[12] L. Khalil, C. Eid, M. Bechelany, N. Abboud, A. Khoury, P. Miele, Mater. Lett. 140 (2015) 27.
[13] Y. Wang, D. Su, A. Ung, J. Ahn, G. Wang, Nanotechnology 23 (2012) 055402/1.
[14] J. Fu, C.J. DeSantis, R.G. Weiner, S.E. Skrabalak, Chem. Mater. 27 (2015) 1863.
[15] B. Wang, G. Wang, Z. Lv, H. Wang, Phys. Chem. Chem. Phys. 17 (2015) 27109.
[16] J. Mao, X. Hou, X. Wang, S. Hu, L. Xiang, Mater. Lett. 161 (2015) 652.
[17] T. Sener, E. Kayhan, M. Sevim, O. Metin, J. Power Sources 288 (2015) 36.
[18] B. Wang, S. Li, X. Wu, B. Li, J. Liu, M. Yu, Phys. Chem. Chem. Phys. 17 (2015) 21476.
[19] Q.Q. Xiong, J.P. Tu, S.J. Shi, X.Y. Liu, X.L. Wang, C.D. Gu, J. Power Sources 256 (2014) 153.
[20] B. Cai, M. Zhao, Y. Ma, Z. Ye, J. Huang, ACS Appl. Mater. Interfaces 7 (2015) 1327.
[21] M. Li, Y.-X. Yin, C. Li, F. Zhang, L.-J. Wan, S. Xu, D.G. Evans, Chem. Commun. 48 (2012) 410.
[22] Y. Xiao, C. Hu, M. Cao, Chem. Eur. J. 19 (2013) 10193.
[23] M. Zhang, Y. Jin, Q. Wen, C. Chen, M. Jia, Appl. Surf. Sci. 277 (2013) 25.
[24] M. Zhang, M. Jia, Y. Jin, Q. Wen, C. Chen, J. Alloys Compd. 566 (2013) 131.
[25] R. Huo, W.-J. Jiang, S. Xu, F. Zhang, J.-S. Hu, Nanoscale 6 (2014) 203.
[26] H. Lv, X. Liang, Y. Cheng, H. Zhang, D. Tang, B. Zhang, G. Ji, Y. Du, ACS Appl. Mater. Interfaces 7 (2015) 4744.
[27] D.-W. Jeong, A. Jha, W.-J. Jang, W.-B. Han, H.-S. Roh, Chem. Eng. J. 265 (2015) 100.
[28] S. Varghese, M.G. Cutrufello, E. Rombi, R. Monaci, C. Cannas, I. Ferino, J. Porous Mater. 21 (2014) 539.
[29] A. Biabani-Ravandi, M. Rezaei, Z. Fattah, Chem. Eng. Sci. 94 (2013) 237.
[30] P. Mountapmbeme Kouotou, H. Vieker, Z.Y. Tian, P.H. Tchoua Ngamou, A. El Kasmi, A. Beyer, A. Galzhauserb, K. Kohse-Hoinghaus, Catal. Sci. Technol. 4 (2014) 3359.
[31] A. Biabani-Ravandi, M. Rezaei, Chem. Eng. J. 184 (2012) 141.
[32] R. Ma, Z. Liu, K. Takada, N. Iyi, Y. Bando, T. Sasaki, J. Am. Chem. Soc. 129 (2007) 5257.
[33] P. Karipoth, A. Thirumurugan, R.J. Joseyphus, J. Colloid Interface Sci. 404 (2013) 49.
[34] A.K. Rai, J. Gim, T.V. Thi, D. Ahn, S.J. Cho, J. Kim, J. Phys. Chem. C 118 (2014) 11234.
[35] E.T. Saw, U. Oemar, X.R. Tan, Y. Dub, A. Borgna, K. Hidajat, S. Kawi, J. Catal. 314 (2014) 32.
[36] D.-W. Lee, M.S. Lee, J.Y. Lee, S. Kim, H.-J. Eom, D.J. Moon, K.-Y. Lee, Catal. Today 210 (2013) 2.
[37] Y.I. Choi, Y.I. Kim, D.W. Cho, J.S. Kang, K.T. Leung, Y. Sohn, RSC Adv. 5 (2015) 79624.
[38] F. Zan, Y. Ma, Q. Ma, Y. Xu, Z. Dai, G. Zheng, M. Wu, G. Li, J. Am. Ceram. Soc. 96 (2013) 3100.
[39] D.M. Clifford, C.E. Castano, A.J. Lu, E.E. Carpenter, J. Mater. Chem. C 3 (2015) 11029.
[40] Y. Sohn, D. Pradhan, J.S. Kang, K.T. Leung, RSC Adv. 5 (2015) 31472.
[41] J.S. Gwag, Y. Sohn, Bull. Korean Chem. Soc. 33 (2012) 505.
[42] J. Chen, X.-H. Xia, J.-P. Tu, Q.-Q. Xiong, Y.-X. Yu, X.-L. Wang, C.-D. Gu, J. Mater. Chem. 22 (2012) 15056.
[43] Y.J. Hong, J.S. Cho, Y.C. Kang, Chem. Eur. J. 21 (2015) 18202.
[44] M. Fu, Q. Jiao, Y. Zhao, H. Li, J. Mater. Chem. A 2 (2014) 735.
[45] S. Li, B. Wang, J. Liu, M. Yu, Electrochim. Acta 129 (2014) 33.
[46] S. Ren, X. Zhao, R. Chen, M. Fichtner, J. Power Sources 260 (2014) 205.
[47] D.P. Dubal, P. Gomez-Romero, B.R. Sankapal, R. Holze, Nano Energy 11 (2015) 377.
[48] B. Wang, Q. Liu, Z. Qian, X. Zhang, J. Wang, Z. Li, H. Yan, Z. Gao, F. Zhao, L. Liu, J. Power Sources 246 (2014) 747.
[49] E. Umeshbabu, G. Rajeshkhanna, G. Ranga Rao, Int. J. Hydrogen Energy 39 (2014) 15627.
[50] Y. Sohn, J. Mol. Catal. A 379 (2013) 59.
[51] W.J. Kim, B.K. Min, D. Pradhan, Y. Sohn, CrystEngComm 17 (2015) 1189.
[52] Y. Park, S.K. Kim, D. Pradhan, Y. Sohn, Chem. Eng. J. 250 (2014) 25.
[53] Y. Park, S.K. Kim, D. Pradhan, Y. Sohn, React. Kinet. Mech. Catal. 113 (2014) 85.
[54] Y. Na, S.W. Lee, N. Roy, D. Pradhan, Y. Sohn, CrystEngComm 16 (2014) 8546.
[55] W.J. Kim, S.W. Lee, Y. Sohn, Sci. Rep. 5 (2015) 13448.
[56] Y.I. Choi, S. Lee, S.K. Kim, Y.-I. Kim, D.W. Cho, M.M. Khan, Y. Sohn, J. Alloys Compd. 675 (2016) 46.